Establishing density-dependent longitudinal sound speed in the vertebral lamina

Rui Xu and Meaghan A. O'Reilly

Citation: The Journal of the Acoustical Society of America **151**, 1516 (2022); doi: 10.1121/10.0009316
View online: https://doi.org/10.1121/10.0009316
View Table of Contents: https://asa.scitation.org/toc/jas/151/3
Published by the Acoustical Society of America

JASA ARTICLE

Establishing density-dependent longitudinal sound speed in the vertebral lamina

Rui Xu[1,a)] and Meaghan A. O'Reilly[2,b)]
[1]Department of Medical Biophysics, University of Toronto, 101 College Street, Suite 15-701, Toronto, Ontario, M5G 1L7, Canada
[2]Physical Sciences Platform, Sunnybrook Research Institute, 2075 Bayview Avenue, Toronto, Ontario, M4N 3M5, Canada

ABSTRACT:
Focused ultrasound treatments of the spinal cord may be facilitated using a phased array transducer and beamforming to correct spine-induced focal aberrations. Simulations can non-invasively calculate aberration corrections using x-ray computed tomography (CT) data that are correlated to density (ρ) and longitudinal sound speed (c_L). We aimed to optimize vertebral lamina-specific $c_L(\rho)$ functions at a physiological temperature (37 °C) to maximize time domain simulation accuracy. Odd-numbered *ex vivo* human thoracic vertebrae were imaged with a clinical CT-scanner ($0.511 \times 0.511 \times 0.5$ mm), then sonicated with a transducer (514 kHz) focused on the canal *via* the vertebral lamina. Vertebra-induced signal time shifts were extracted from pressure waveforms recorded within the canals. Measurements were repeated 5× per vertebra, with 2.5 mm vertical vertebra shifts between measurements. Linear functions relating c_L with CT-derived density were optimized. The optimized function was $c_L(\rho) = 0.35(\rho - \rho_w) + c_{L,w}$ m/s, where w denotes water, giving the tested laminae a mean bulk density of 1600 ± 30 kg/m^3 and a mean bulk c_L of 1670 ± 60 m/s. The optimized lamina $c_L(\rho)$ function was accurate to $\lambda/16$ when implemented in a multi-layered ray acoustics model. This modelling accuracy will improve trans-spine ultrasound beamforming.
 https://doi.org/10.1121/10.0009316
(Received 18 August 2021; revised 25 November 2021; accepted 26 December 2021; published online 7 March 2022)
[Editor: Keith A. Wear] Pages: 1516–1531

I. INTRODUCTION

Focused ultrasound is a non-invasive therapeutic approach that directs ultrasound energy deep into tissues to elicit a range of bioeffects depending on the ultrasound exposure parameters and the intravenous administration of ultrasound contrast agents. This technology shows promise for improving drug delivery to the spinal cord in small animal models.[1–7] However, focusing ultrasound through human vertebrae is a challenge due to their larger dimensions and higher densities. The spine aberrates the incident ultrasound wavefront and distorts the intended focus.[8] This is a similar challenge to skull-induced focal distortions in ultrasound brain therapies.[9] For the skull, sound speed has been related to computed tomography (CT)-derived bone mineral density[10–15] to establish density-dependent relationships that can be used for treatment planning using patient-specific numerical models. These models allow for bone-induced phase and amplitude aberrations to be corrected using phased arrays[16–20] or acoustic lenses.[21,22] In the brain, the transcranial ultrasound technology is sufficiently advanced, and thermal ablation treatments for essential tremor and Parkinson's disease have received regulatory approval,[20,23] while low power exposures for transiently opening the blood brain barrier are in clinical trials.[24,25] Opportunities exist to extend the utility of these treatments to the spinal cord, enabling treatment of the entire neuroaxis, but approaches and models for targeting ultrasound through the intact spine have received less attention than their transcranial counterparts. By building on methods developed for transcranial focused ultrasound, here, we extract spine-specific parameters to improve the accuracy of transspine ultrasound simulation.

Accurately calculating spine-specific aberration corrections requires a simulation model derived from patient-specific spine geometries that incorporates accurate acoustic properties of the spine. A multi-layered ray acoustics simulation based on CT images of human vertebrae was adapted from transcranial modelling and the spatial accuracy was evaluated for trans-vertebral ultrasound propagation.[8] In this model, sound is propagated from a layer that represents the transducer face to a layer representing the posterior vertebra interface, then through the posterior arch to a layer representing the inner vertebral canal interface, then finally into the vertebral canal. The ray acoustics model used relationships between CT-derived voxel density (ρ) and skull acoustic properties to build the simulation domains.[8,11,12] Clinical-resolution CT-derived density has been correlated to the heterogeneous acoustic properties of skulls using continuous linear and non-linear models, and used for clinical treatment planning for transcranial focused ultrasound procedures.[10–15,26] The skull acoustic properties were accurate enough for the ray acoustics model to reproduce the spatial pressure distributions of sound focused through the posterior arch of human thoracic vertebrae.[8,11,12] However, the ray

a)Electronic mail: xurui.xu@mail.utoronto.ca, ORCID: 0000-0003-1606-0932.
b)ORCID: 0000-0003-2889-6614.

https://doi.org/10.1121/10.0009316

acoustics model in Xu and O'Reilly[8] was not validated in the time domain and it is crucial that the model be able to accurately calculate vertebra-induced time shifts for future use in trans-spine focusing. Optimal trans-spine focusing will likely require focusing ultrasound through the vertebral laminae (translaminar propagation) and focusing ultrasound through the acoustic windows between laminae (paralaminar propagation).[27] The difference in sound speed between the soft paralaminar tissues and the bony vertebral lamina can result in larger signal time shifts than those resulting from propagation through different parts of the posterior arch alone, increasing the importance of accurately characterizing the sound speed in the vertebral lamina.

There are several reasons why sound speed in vertebral laminae may differ from skull. Trabecular orientation affects the speed of sound in bone.[28–31] Unlike in skull bone, the trabecular network is anisotropic in the vertebral posterior arch as a result of loading by the tendons and ligaments encapsulating the vertebral column.[32,33] The laminar cortical shell also provides structural support to the vertebral column[34,35] and may differently influence the cortical microstructure and corresponding acoustic properties. The mechanical demands placed on the posterior arches of thoracic vertebrae may result in a bone morphology and anisotropy and corresponding speed of sound that differs from that of skull. The objective of this work is to optimize the relationship between CT-derived density and longitudinal sound speed in the vertebral laminae (c_L) in order to validate the ray acoustics model in the time domain for transvertebral ultrasound propagation.

Vertebra lamina thickness, composition, and microstructure varies within each vertebral posterior arch and between vertebrae.[33] Variability in laminar thickness precludes the use of methods that use a uniform measured thickness to determine a bulk speed of sound,[36,37] instead requiring the coupled approach of simulation-based optimization with empirical measurements. Case-specific simulation with CT-derived bone geometry, density maps, and corresponding acoustic property maps have been used to account for irregular and heterogeneous bone structures in previous efforts of determining the speed of sound in skull.[10–13] In this study, the main objective was to optimize vertebra-specific speed of sound functions. Mode conversion at the vertebra interfaces results in two propagated waves: a longitudinal wave, and a shear wave. In this study, the speed of the shear mode was set to a constant fraction (1400/2550, giving a realistic Poisson's ratio of 0.28[38]) of the speed of the longitudinal mode, halving the number of optimization parameters, and remaining consistent with previous work in skull.[39,40] We performed a grid search to optimize a density-longitudinal sound speed model to maximize simulation accuracy in predicting phase shifts induced by vertebral lamina at a clinically relevant frequency. A multi-layered ray acoustics model was used in the grid search to simulate translaminar ultrasound propagation and calculate vertebra-induced phase shifts. This model accounted for bone heterogeneity with voxel-specific transmission coefficients and path-averaged complex wavenumbers.[8]

II. METHODS

A. Vertebral specimen

A dehydrated *ex vivo* adult human spine (Osta International, White Rock, BC, Canada) was rehydrated by extensively degassing the vertebrae in de-ionized water then submerging the vertebrae in 10% neutral buffered formalin for several months. Dessication and rehydration can result in a small increase in longitudinal sound speed (2.3% in porcine skull[41]) but the buffered formalin has negligible effect on sound speed.[9] The dimensions of the vertebral bodies were compared to Limthongkul *et al.*,[42] and the average vertebral body volume was 5.4% smaller than the average male specimen and 7.2% larger than the average female specimen. No obvious signs of vertebral pathology were present other than some minor ossification of the ligamentum flavum in T10, which was not included in this study but could indicate an advanced age. The vertebrae were degassed in a vacuum chamber (Nalgene vacuum chamber, Fisher Scientific; Gast, Benton Harbor, MI, USA) for several hours prior to imaging with a clinical CT scanner (Aquilone One, Toshiba). The vertebrae were oriented with the vertical axis aligned with the CT bore, as if they were *in vivo*. The vertebrae were then imaged with a resolution of 0.511 mm $\times$ 0.511 mm in plane and 0.5 mm slice thickness. The CT settings that were used were those previously used for skull (reconstruction kernel: FC30, 120 kVP), as beam energy and reconstruction method can affect CT intensity,[14,20,43–45] although the scanner vendor and reconstruction kernel did not cause obvious differences in optimized acoustic properties in McDannold *et al.*[15] The clinical CT scanner was used to match a future clinical workflow, where a pre-operative CT scan is used to obtain geometry and acoustic properties for patient-specific simulation-based aberration corrections. This limited the resolution of the CT image to 0.5 mm, larger than trabecular structure (0.1–0.3 mm),[46] which meant that trabecular orientation was lost at this resolution. The odd-numbered thoracic vertebrae (T1, T3,… T11) were used for this experiment. Horizontal slices of the vertebrae and the distributions of CT-derived voxel densities of the posterior vertebral arch are displayed in Fig. 1.

Experiments were performed in a scan tank filled with degassed and de-ionized water (Fig. 2), heated to 37 °C using an immersion circulator (Polystat Standard Immersion Circulator, Cole-Parmer, Montreal, QC, Canada). The vertebrae were clamped at the anterior edge of the vertebral body and positioned using a manual 3-axis positioning system such that the geometric focus of the transducer was at the centre of the vertebral canal and the transducer axis was oriented to focus through the vertebral lamina (approximately 30° vertebra rotation around the longitudinal axis, away from the anteroposterior, AP, axis). One lamina was tested per vertebra. An example of the transducer-vertebra configuration is shown in Fig. 2(a). The vertebrae were shifted by a total of 10 mm in 2.5 mm increments along the vertical axis [z-axis, Fig. 2(c)] using a stage micrometer giving a total of five transducer-vertebra configurations per vertebra.

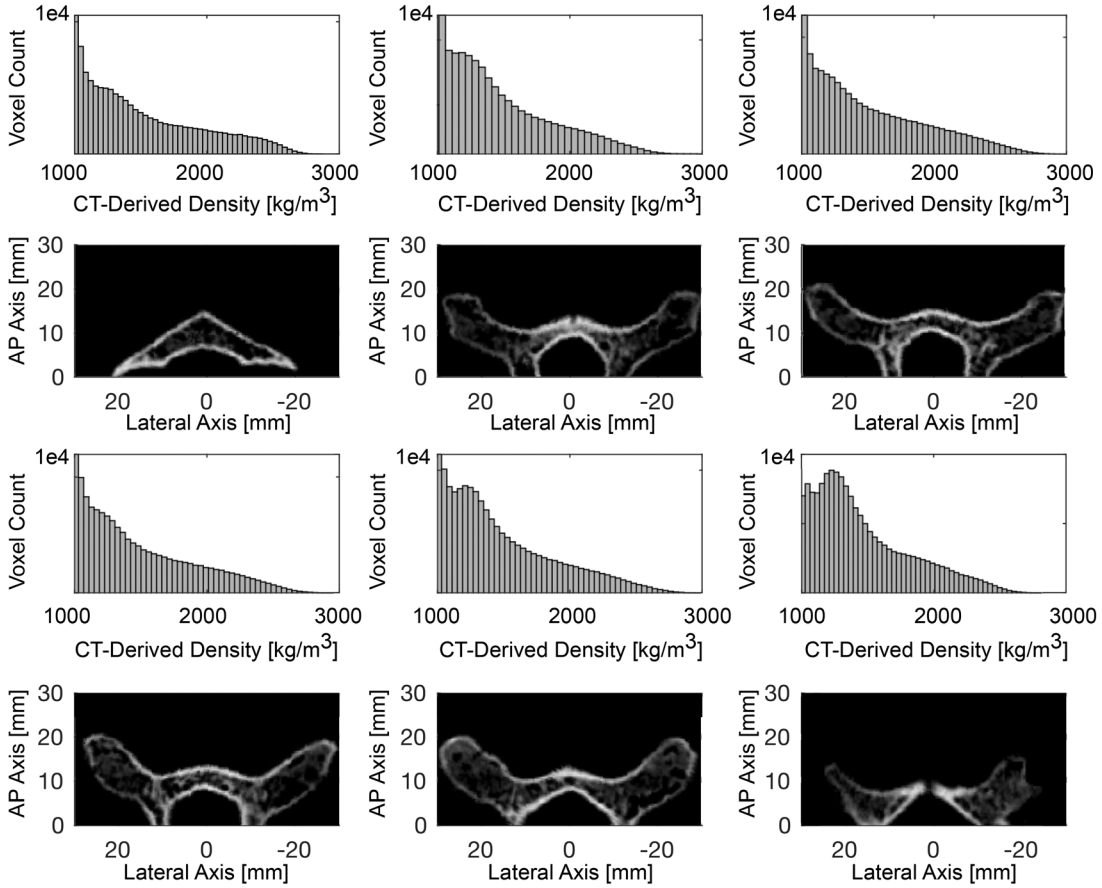

FIG. 1. Distributions of voxel densities for the posterior arches of the *ex vivo* thoracic vertebrae (T1, T3, … T11) used in this experiment. Density units, kg/m^3. Anterio-posterior (AP), lateral slices of the *ex vivo* vertebrae in degassed and de-ionized water showing the laminae and spinous process, when possible. Grayscale limits: 998–3000 kg/m^3.

B. Sonication parameters

A custom 5 cm diameter, 6 cm focal length spherically focused piezocomposite transducer with a fundamental frequency of 514 kHz was used to sonicate the *ex vivo* human vertebrae. The frequency was chosen to balance the trade-off between focal size and attenuation.[47] The transducer was fixed in place. The transducer was driven with a single cycle pulse (Pulse Repetition Frequency: 1 kHz, Function Generator: Tektronix AFG3052C, Amplifier: NP Technologies model NP-2519) at an amplitude below the threshold of non-linear effects (no visible harmonics in the frequency domain in the measured waveforms) and peak negative pressures at the focus in water below 0.4 MPa. An example of time domain pressure is shown in Fig. 3, both in water and after propagating through the lamina of a vertebra. The short pulse was chosen to prevent standing wave formation, but results in a pulse with a –3 dB bandwidth of 120–130 kHz centered at 514 kHz, calculated with powerbw in MATLAB 2020a from signals recorded at the geometric focus in the vertebral canals.

A needle hydrophone (Precision Acoustics, 0.5 mm diameter), oscilloscope (Tektronix MDO3014), and electronic three-axis positioning system (Velmex) were used to measure pressure waveforms within the vertebral canal at a sampling rate of 250 MS $\cdot$ s^{-1} (40 μs, 1×104 samples). The hydrophone was aligned at 90° relative to the axis of the transducer, with the tip of the hydrophone facing in the +z direction to allow pressure measurements to be made in the vertebral canal.[8] This is against Precision Acoustics guidelines, which asks that the needle tip be oriented directly towards the source. However, it has been shown that for the given needle geometric radius $a_g = 0.25$ mm and transducer wavenumber in water $k = 2\pi f/c$, that for $k \times a_g \approx 0.5$, that (extrapolating experimental measurements from 70° to 90°), the hydrophone directivity remains over 0.7 at 90°, sufficient for this experiment.[48] The positioning system was used to measure pressure waveforms in $6.5 \times 6.5 \times 6.5$ mm^3 volumes centered at the geometric focus of the transducer within the vertebral canal. The step size for the planar scans was 0.5 mm, giving 14^3 waveform measurements per experiment. The needle hydrophone tip was used to record the position of nine anatomical markers on the superior vertebra surface for each vertebra position shown in Fig. 2(a) for the purpose of generating the affine transformation required to register the simulation space to the experiment space.

C. Time-shift extraction

The pressure raster scans were first performed in water, then in the vertebral canal. The water scans were performed in order to obtain baseline voxel-wise waveforms for

https://doi.org/10.1121/10.0009316

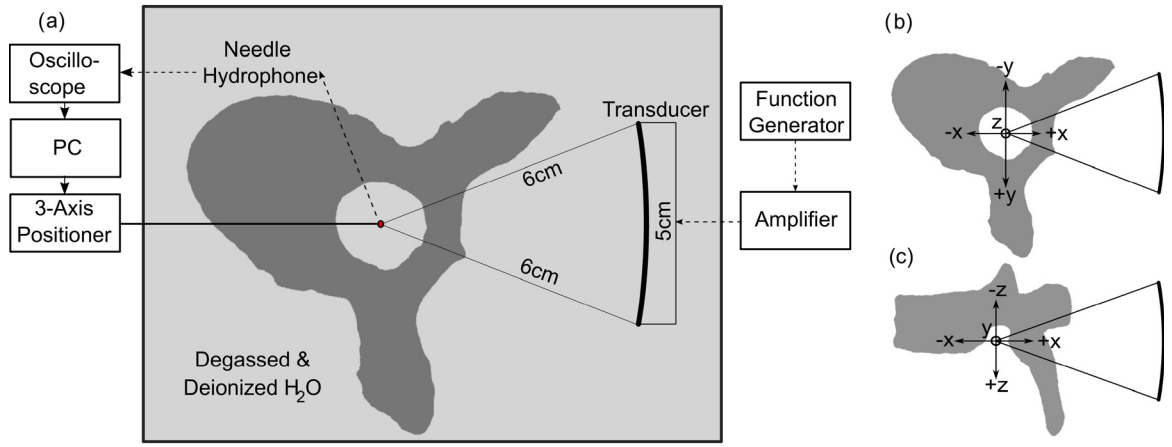

FIG. 2. (Color online) (a) Experimental setup, with an example transducer-vertebra configuration. The coordinate system is based on the geometric focus of the transducer. (b) Superior view of the coordinate system. (c) Lateral view of the coordinate system. Rubber-lined tank dimensions are $x = 90$ cm, $y = 30$ cm, and $z = 30$ cm. The transducer and vertebra are presented to scale relative to one another.

comparison with the waveforms modified by the insertion of the vertebra. Figure 4 displays a two-dimensional (2D) slice of the spatial distribution of maximum pressure amplitude of the water waveforms $p_w(t)$ and the vertebra canal waveforms $p_v(t)$. The voxel-wise vertebra induced time-shift τ was calculated by maximizing the cross correlation of the time-domain pressure signals $p_w(t)$ and $p_v(t)$:

$$\tau = \text{argmax}((p_w * p_v)(t)). \tag{1}$$

The time-shift τ is the group time shift; phase shifts and corresponding phase velocities were not investigated. The maximized signal correlation,

$$s_c = \sum p_v(t) p_w(t+\tau), \tag{2}$$

describes the similarity between $p_v(t)$ and $p_w(t+\tau)$, and is maximized when the vertebra does not distort the waveform.

We expected the reliability of τ measurements to be maximized when s_c is high. The spatial distribution of normalized signal correlation $\tilde{s_c}$ is shown in Fig. 4, and the peak coincides with the focal maximum. Normalization, $\tilde{s_c} = 2s_c/(p_v^2 + p_w^2)$, was necessary to account for spatial variance in amplitude of the time domain waveforms. Normalized cross correlation is able to generate a precise estimate of the time shift as it accounts for the energy of the two signals, albeit at a relatively high computational cost.[49]

Figure 4 shows an example of vertebra insertion, resulting in the distortion of the ultrasound focus. Signal correlation was also maximized in the focal region, where signal intensity was highest. Figure 3 shows the method used to extract τ for the maximum $\tilde{s_c}$ measured in the 2D scan displayed in Fig. 4.

D. Ray acoustic propagation model

A multi-layered ray acoustics model was used to simulate the vertebra-induced phase shift. The model and the accuracy of this model is described in Xu and O'Reilly.[8] The affine transformation calculated from the anatomical markers measured with the needle hydrophone tip and the anatomical markers measured on the vertebra mesh generated from the CT data were used to rotate and translate the CT data and mesh into the experimental transducer-vertebra configuration with minimal change to the density distribution and spatial distribution of the voxels. The ray acoustics model calculates a complex pressure p at every empirical measurement point r, from which the phase shift $\phi_s(r)$ is calculated on a voxel-wise basis using

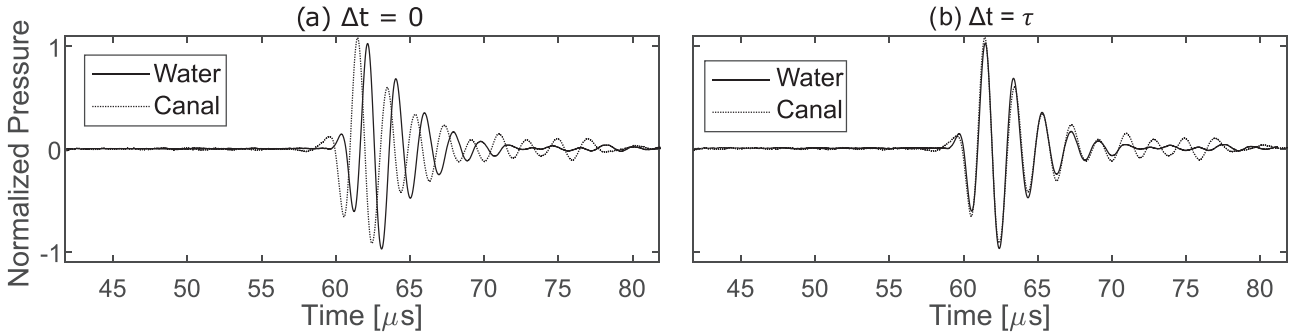

FIG. 3. A water and canal signal with a normalized maximum cross correlation of $\tilde{s_c} = 0.97$ are shown in (a) $\Delta t = 0$ and (b) $\Delta t = \tau$, where Δt is the shift in the water signal and $\Delta t = \tau$ is the shift that maximizes signal cross correlation.

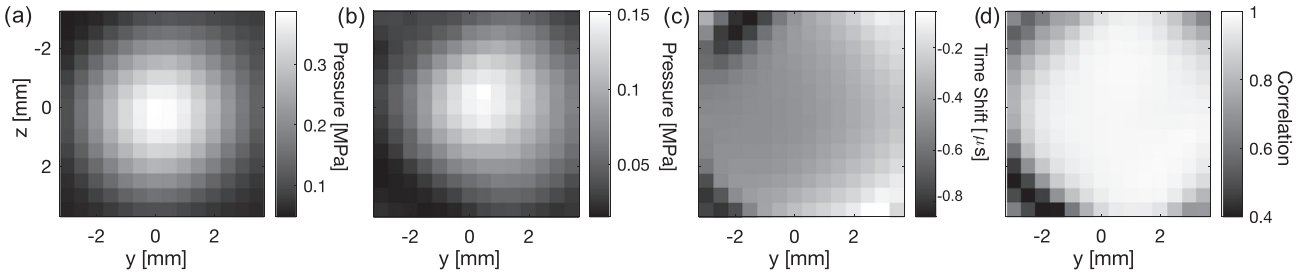

FIG. 4. (a) Focal pressure distribution (water). (b) Focal pressure distribution (canal). (c) Voxel-wise vertebra-induced time shift. (d) Normalized voxel-wise water-canal signal cross correlation. All images are of the YZ plane.

$$\phi_s(r) = \text{atan2}\left(\frac{p_v(r)}{|p_v(r)|}\right) - \text{atan2}\left(\frac{p_w(r)}{|p_w(r)|}\right), \tag{3}$$

where $p_v(r)$ and $p_w(r)$ are the simulated pressures with the vertebra and without the vertebra (water only), respectively, and atan2 is the MATLAB four-quadrant inverse tangent function. The ray acoustics model generates a steady-state solution and can only be compared to the empirical phase shift $\phi_e(r) = \omega\tau(r)$ if the empirical phase shift is constrained to within one wavelength, $[-\pi, \pi]$. For a centre frequency of $f = 514$ kHz, and a bone thickness of $d = 5$ mm, the maximum average change in the speed of sound (Δc) relative to water ($c_0 = 1524$ m/s at 37°) through bone that can be converted to ϕ_e and compared to ϕ_s is

$$\Delta c = \frac{c_0 f d}{f d - c_0} - c_0, \tag{4}$$

which, for the assumed parameters, is $\Delta c \approx 2200$ m/s, giving a maximum allowed average bone c_L of approximately 3700 m/s. Given that the bulk longitudinal speed of sound in bone in the literature is generally between 2500 and 3000 m/s,[50] the maximum speed of sound $c = c_0 + \Delta c$ used in this method should be sufficient. However, issues with this approach arise with higher frequencies and greater bone thicknesses, although the validity of this approach is extended when the shear mode becomes dominant, as the shear speed of sound is much closer to that of water.

Figure 5(f) describes simulation error in predicting phase shift at the focus ($I > 0.5I_{\max}$, where I_{max} is the maximum intensity in the experiment measurement domain). The intensity threshold was implemented to remove potentially poorly correlated signal shifts and to emphasize time shifts at the focus. The phase error of the simulation constitutes the quantity to be minimized by optimizing the $c_L(\rho)$

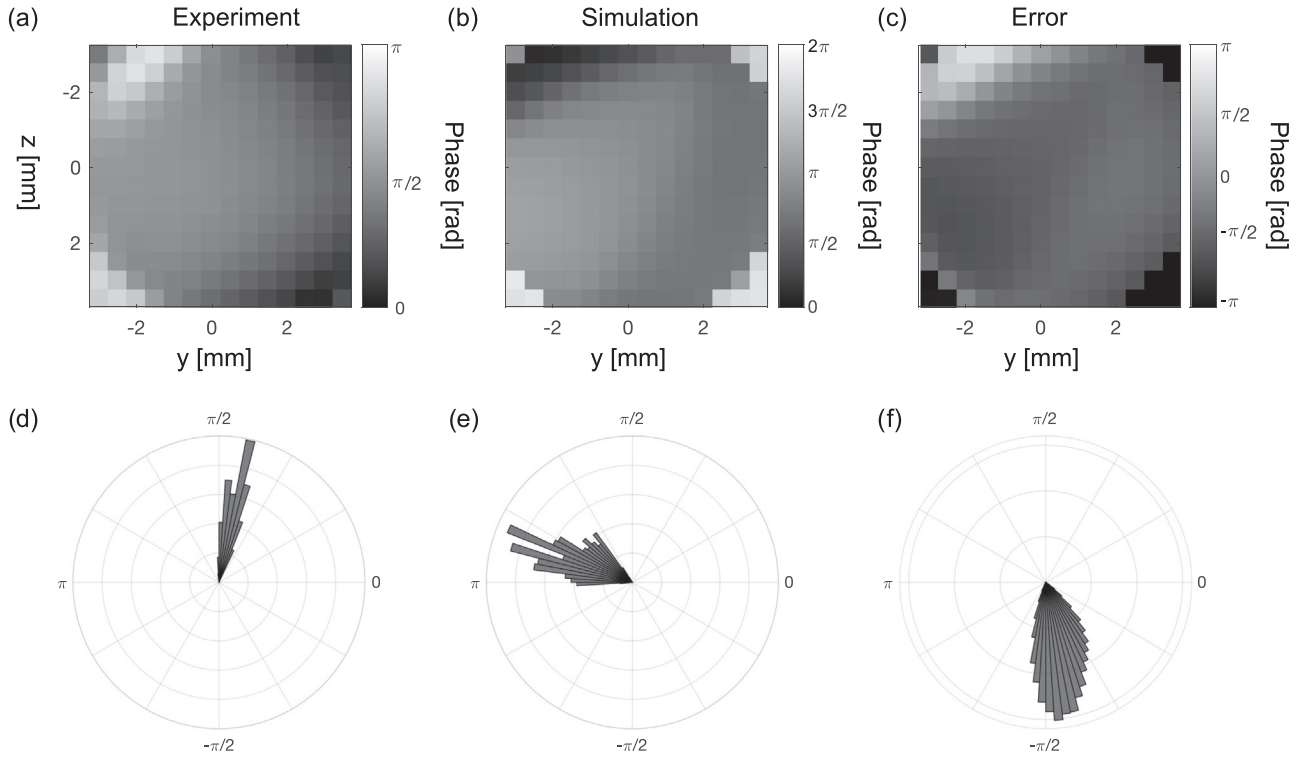

FIG. 5. Phase comparison for the experimental results displayed in Fig. 4. Top, from left: spatial distribution of experimental phase shift, simulated phase shift (skull acoustic properties), and simulation phase error. Bottom: corresponding phase distributions for voxels with $I > 0.5I_{\max}$, where I_{max} is the maximum intensity in the experiment measurement domain.

https://doi.org/10.1121/10.0009316

function. As previously mentioned, the shear speed of sound, c_S was set as a constant ratio of the longitudinal speed of sound, c_L, $c_S = (1400/2550)c_L$. Longitudinal attenuation was not optimized but was included for accuracy in modelling the sound received from different paths. The longitudinal attenuation coefficient, α_L was interpolated from the functions optimized in Ref. 11 at 270 and 836 kHz. The shear attenuation coefficient, α_S, was set as a constant proportion of the longitudinal attenuation coefficient: $\alpha_S = (90/85)\alpha_L$.[39] Longitudinal and shear attenuation coefficient optimization could be the subject of a future investigation.

E. Vertebra lamina thickness

Intra-laminar and intervertebral differences in lamina thicknesses were estimated using the mesh models generated for the multi-layered ray acoustics model to determine if a correlation existed between lamina thickness and vertebra-induced signal time shifts. The mesh elements within a 5 mm radius cylinder of the transducer propagation axis were isolated from the mesh. This encompasses most of the contributing elements to the pressure received within the canal, evaluated trigonometrically using the geometry of the transducer. Mesh elements with normals that deviated by more than 60° away from the transducer axis of propagation were removed from the mesh in order to isolate two surfaces that were close to plate-like in geometry. Elements with angles greater than 60° away from the transducer axis were assumed to not contribute significantly due to being well beyond the longitudinal critical angle and approximately at the shear critical angle. The distances from a, a mesh element in the transducer-side surface, to the elements on the canal-side surface (within a 0.5 mm radius cylinder defined by the normal of a) were calculated. This process was repeated for all a to obtain an estimate of the mean and standard deviation in arch thickness in the area where the transducer beam intersects the bone. Figure 6 shows the process by which mesh elements are extracted from the vertebra mesh from the inner and outer surfaces of the vertebral lamina.

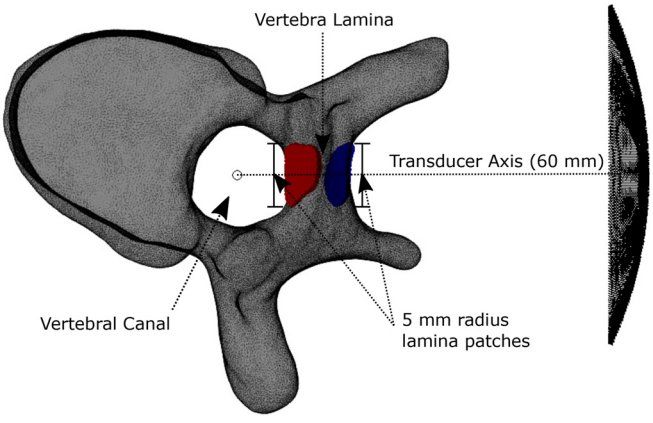

FIG. 6. (Color online) Vertebra lamina thicknesses were calculated from coaxial 5 mm radius circular patches of mesh elements extracted from the vertebra mesh along the transducer propagation axis.

F. Longitudinal vs shear transmission

The multi-layered ray acoustics model allowed shear and longitudinal modes to be simulated independently, enabling the calculation of the proportion of sound that reached the canal that was propagated separately through longitudinal and shear modes in the vertebrae. Ultrasound velocities at the mesh elements in the bone interface of the vertebral canal were extracted using the same method as applied to obtain the arch thickness; by excluding elements outside a cylinder with 5 mm radius connecting the center of the transducer to the origin. The individual mesh element velocities were then multiplied by the individual element areas (the areas of the elements are not identical), then divided by the total area of the remaining elements in the mesh.

G. Optimization cost function

We defined the optimization cost function as a function of phase error, (ϕ_ϵ), the difference between experiment phase (ϕ_e) and simulation phase (ϕ_s), $\phi_\epsilon = \phi_e - \phi_s$. Both experiment and simulation phases are converted to radians. We defined the cost function as a weighted sum of squared phase errors, where the errors are weighted by intensity,

$$\Phi = \frac{1}{4\pi^2 M}\sum_{i=1}^{M} I_i \phi_\epsilon^2, \tag{5}$$

where M is the number of measurement/control points and I_i is the intensity at each measurement point. The phase errors were weighted by acoustic intensity to increase the weighting of the cost function at the focus, where the waveform was most coherent and signal cross correlation was maximized, giving the most accuracy in empirical signal time shifts (Fig. 4). The control points were restricted to measurement points with $I_i > 0.5 \times I_{\max}$, where $I_{\max}$ was the maximum intensity in the waveform volume, in order to avoid using signal time shifts extracted from poorly correlated data.

H. Linear models

Two main approaches have been used to model speed of sound as a function of CT-derived density: linear models[12–14] and spline-based models.[10,11] We began with a simple line search and a set of linear functions relating the longitudinal group velocity to the CT-derived density in the posterior vertebral arch. The linear functions are forced through the speed of sound in water at the CT-derived density of water,

$$c_L(\rho) = \mathrm{m}(\rho - \rho_w) + c_{L,w}, \tag{6}$$

where ρ_w is the density of water, $c_{L,w}$ is the longitudinal speed of sound in water, and m is the slope and the sole

optimization parameter. The range of tested m was between 0 and 3, and the resulting $c_L(\rho)$ are displayed relative to the data from Pichardo *et al.*,[11] interpolated to 514 kHz, and Marsac *et al.*[13] Linear models that do not force $c_L(\rho_w) = c_{L_w}$ can generate smaller errors due to the increase in fitting parameters of the model, however, these models may then become unphysical.[14]

III. RESULTS

A. Experimental measurements

The time shifts for the tested vertebrae (voxels exceeding 50% of the maximum pressure) at room temperature are displayed in Fig. 7. Intra-arch variance in bone morphology resulted in the variation in the time shifts with changes in vertebra-transducer configuration. Contributors to variation in the time shifts include the thickness of the bone, variation in the surface angles of the bone in the propagation path that results in differing degrees of mode conversion, and differing bone densities along different paths.

Vertebra lamina thickness was extracted from each of the vertebra laminae for each of the transducer-vertebra configurations. The thicknesses are summarized in Fig. 8, and the time shifts and arch thicknesses for each room temperature transducer-vertebra configuration are summarized in Table I. The arch thickness was reported as zero in cases where the beam does not intersect bone or only intersects bone with angles that do not support transmission.

Correlations were calculated between median lamina thicknesses and median vertebra-induced time shifts. The correlations (R) between median thicknesses and median shifts were negatively correlated but were not significant (T1, R = –0.86, $p = 0.06$; T3, R = –0.96, $p = 0.008$; T5, R = –0.45, $p = 0.45$; T7, R = –0.72, $p = 0.17$; T9, R = −0.86, $p = 0.06$; T11, R = −0.99, $p = 2 \times 10^{-4}$). When evaluating the correlation between median thickness and median shift for the entire group of vertebrae and all experiments, the correlation coefficient was –0.34, with $p = 0.07$. The median lamina thickness along the transducer propagation path and the median vertebra-induced time shift are plotted against one another in Fig. 9.

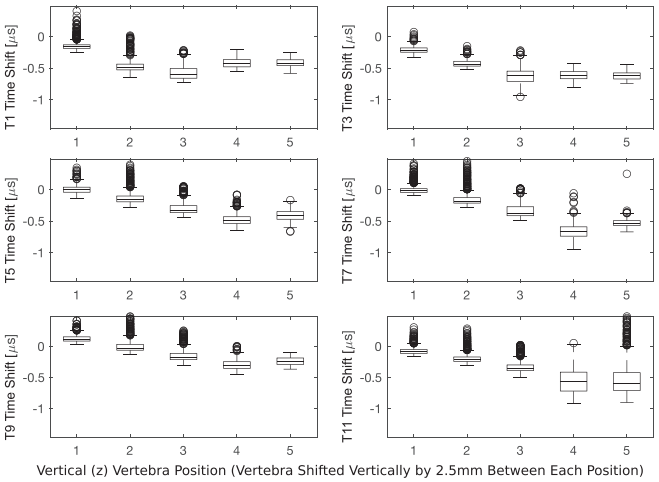

FIG. 7. Experimentally measured vertebra-induced signal time shifts. Box and whisker plot showing the range, median value, interquartile range. Outliers are represented with circles.

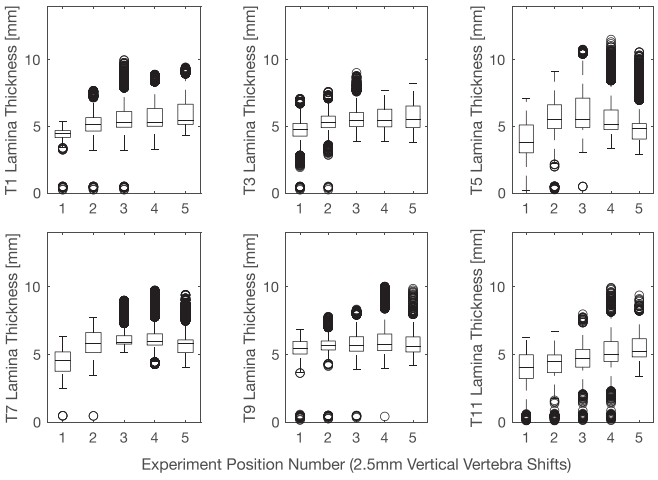

FIG. 8. The thickness of the laminae along the propagation paths of the transducer in five different positions. Box and whisker plot showing the range, median value, interquartile range. Outliers are represented with circles.

The linear fit in Fig. 9 returns a time shift of –0.31 μs for a thickness of 5.4 mm, the overall median lamina thickness of all experiments. The linear fit at 5.4 mm corresponds to a bulk sound speed of 1670 m/s in the lamina, calculated using $c_L = (1/\Delta d \times (\Delta t + \Delta d/c_w))^{-1}$, where $\Delta t = -0.31\mu$s, $\Delta d = 5.4$ mm, and $c_w = 1524$ m/s. Figure 9 shows that the range in time shifts at the median lamina thickness is 0.77 μs, [–0.66, 0.11]μs, or approximately 0.4λ at 514 kHz, and the linear fit is consequently too inaccurate to be used as a method to obtain vertebra-induced time shifts for aberration correction. The range of time shift for given lamina thicknesses may be attributed to mode conversion at the irregular bone interfaces, refraction due to non-normal incident angles, and heterogeneity in the bone properties. Figure 9 and the correlations between vertebra lamina thickness and vertebra-induced time shifts show that vertebra arch thickness alone is insufficient to calculate the vertebra-induced time shifts, and that a model that incorporates medium heterogeneity and mode conversion is required.

B. Ray acoustics: Initial model accuracy

The multi-layered ray acoustics model was used to calculate pressure in the same positions as measured in the experiment using skull acoustic properties.[11,12] Simulation root mean square error in pressure (p_{RMS}) and zero-lag pressure cross correlation (p_{XC}) was calculated for each of the transducer-vertebra configurations in the same manner as in Xu and O'Reilly[8] to ensure that the vertebra registration in simulation was sufficiently accurate. These two image similarity metrics describe the accuracy of the simulation in reproducing pressure values (p_{RMS}), and to reproduce the pressure spatial distribution with robustness to changes in overall

https://doi.org/10.1121/10.0009316

TABLE I. Median and standard deviation in vertebral lamina thicknesses (Δd [mm]) and vertebra-induced time shifts (Δt [μs]) for T1, T3,… T11 for each vertebra-transducer configuration.

		Pos.1	Pos.2	Pos.3	Pos.4	Pos.5
T1	Δd	4.4 ± 0.5	5.2 ± 0.8	5.3 ± 1.1	5.3 ± 1.1	5.4 ± 1.1
	Δt	−0.17 ± 0.06	−0.46 ± 0.13	−0.60 ± 0.08	−0.43 ± 0.04	−0.43 ± 0.04
T3	Δd	4.8 ± 0.9	5.3 ± 0.7	5.5 ± 0.7	5.5 ± 0.9	5.5 ± 1.0
	Δt	−0.24 ± 0.04	−0.44 ± 0.07	−0.66 ± 0.06	−0.63 ± 0.05	−0.63 ± 0.04
T5	Δd	3.8 ± 1.4	5.5 ± 1.5	5.6 ± 1.5	5.1 ± 1.4	4.9 ± 1.3
	Δt	−0.03 ± 0.03	−0.17 ± 0.12	−0.27 ± 0.13	−0.51 ± 0.06	−0.44 ± 0.04
T7	Δd	4.5 ± 0.9	5.8 ± 1.0	5.9 ± 0.7	6.0 ± 1.0	5.8 ± 0.9
	Δt	−0.04 ± 0.05	−0.19 ± 0.12	−0.31 ± 0.13	−0.67 ± 0.07	−0.54 ± 0.03
T9	Δd	5.5 ± 0.9	5.6 ± 0.7	5.6 ± 0.8	5.8 ± 1.0	5.6 ± 0.8
	Δt	0.11 ± 0.04	−0.03 ± 0.11	−0.1 ± 0.15	−0.33 ± 0.06	−0.24 ± 0.05
T11	Δd	4.1 ± 1.4	4.5 ± 1.2	4.7 ± 1.2	5.0 ± 1.4	5.2 ± 0.9
	Δt	−0.10 ± 0.04	−0.23 ± 0.09	−0.38 ± 0.00	−0.49 ± 0.19	−0.61 ± 0.21

pressure intensity (p_{XC}).[51] Table II reports p_{RMS} and p_{XC}, averaged across the five experiment positions, for each vertebra, and for all measurement positions within the measurement volumes. The p_{RMS} and p_{XC} values for the vertebrae and positions tested in this experiment improved on the values reported in Xu and O'Reilly,[8] and so it was assumed that the multi-layered ray acoustics model and vertebra registrations were sufficiently accurate to proceed with the simulation-based optimization of sound speed in the vertebral lamina.

Figure 10 shows axial slices of the simulated and experimentally measured pressure profiles for all of the tested vertebrae and all of the tested transducer-vertebra configurations. The congruence between simulation and experiment is reported in Table II.

C. Ray Acoustics: Linear models

Figure 11 displays the cost functions for each of the tested vertebrae as a function of the slope of the linear model, along with the linear models that minimize those cost functions. The minimum of each cost function and the corresponding optimal slope for each vertebra is reported in Table III. The optimized linear models are plotted relative to two skull models: the interpolated spline from Pichardo *et al.*[11] and the optimized linear model from Marsac *et al.*[13]

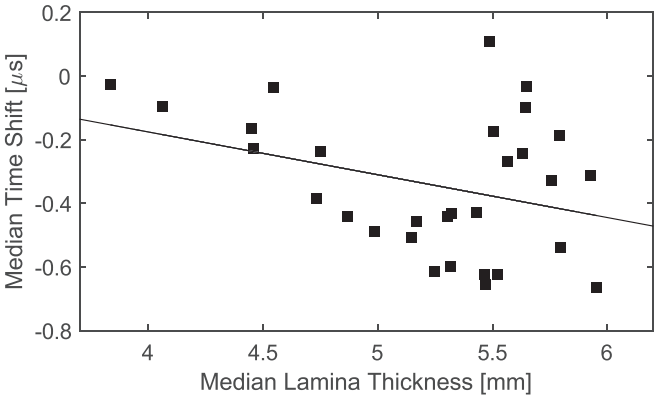

FIG. 9. Lamina thickness vs median vertebra-induced time of flight shifts for six vertebrae (T1, T3, … T11). Five different vertebra positions were tested per vertebra (separated by 2.5 mm, vertically), giving 30 total thickness-time shift pairs. A linear fit was added to the data.

The cost functions displayed in Fig. 11 have two minima, one at a low slope below 0.5 m^4/(s kg), and one at a high slope above 2.5 m^4/(s kg). The high m minima may be due to phase wrapping, or due to shear mode dominance as a result of high sound speeds at the interface creating small longitudinal critical angles. The bulk sound speeds at the high cost function minima are approximately 1600 m/s faster than at the low minima, not quite fast enough to cause phase wrapping at bone thickness of 5 mm, but may cause phase wrapping at higher bone thicknesses. The maximum speed of sound at the high cost function minima is approximately 6500 m/s, corresponding to a longitudinal critical angle of 13°, which is restrictive and unrealistic for the maximum sound speed. In contrast, the maximum speed of sound at the low cost function minima is approximately 2200 m/s, corresponding to a critical angle of 42°, permitting longitudinal mode propagation for a much larger range of incident angles. The absolute minima of all cost functions in Fig. 11 were all located at the low slopes [below 0.5 m^4/(s kg)]. The low slopes correspond to the small time shifts and the slow sound speed extracted using the linear fit in Fig. 9, and the low slope values were used accordingly. Table III displays the mean CT-derived density of the vertebra laminae (mean of all voxels in the vertebra laminae that exceed 998 or 1200 kg/m^3 to exclude partial volume effects and for comparison with work that uses the same threshold[11]) the minima in cost function, Φ_{min}, are displayed for each vertebra for the linear models, along with the corresponding slopes associated with Φ_{min} for the linear functions. The slope of T9 is the lowest of the tested vertebrae and the cost function for T9 is the highest, suggesting that in this case, a linear $c_L(\rho)$ model does not work as well.

TABLE II. Root mean square error (p_{RMS}) and zero-lag cross correlation (p_{XC}), calculated from the five transducer-vertebra positions per tested vertebra, and across all tested vertebrae.

	T1	T3	T5	T7	T9	T11	Total
p_{RMS}[%]	1.1 ± 0.7	2 ± 2	2 ± 1	1.4 ± 0.6	3 ± 2	2 ± 1	2 ± 1
p_{XC} [%]	91 ± 6	94 ± 4	97 ± 2	95 ± 1	97 ± 1	95 ± 4	95 ± 4

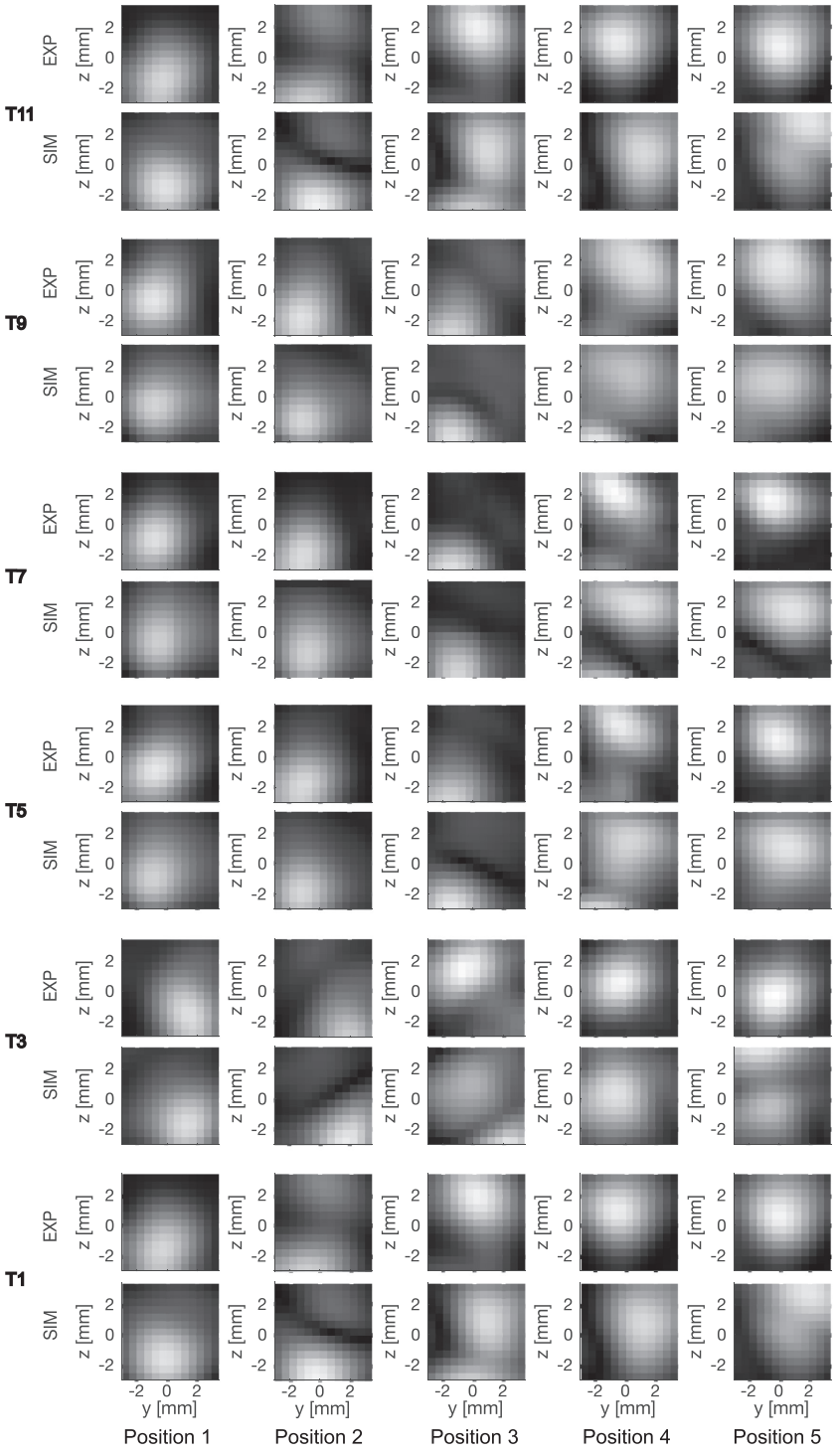

FIG. 10. Axial slices of the simulated (skull acoustic properties) and experimentally measured pressure profiles within the vertebral canal, for all tested vertebra-transducer configurations.

Figure 11 shows that the optimized speed of sound functions for the vertebrae provide slower sound speeds than skull for a given voxel density. The distributions of voxel densities in the posterior vertebral arches differs from those of skulls, so comparisons with work that reports bulk and/or arithmetic mean speed of sound in skulls requires calculating the bulk and arithmetic mean speeds of sound in our vertebral posterior arches. The arithmetic mean speed of sound ($\overline{c_L}$) in the posterior arch was calculated with the optimized vertebra linear models. The bulk speed of sound (c_{av}) was calculated for comparison with work that reports this metric in lieu of the mean speed of sound, i.e., Connor *et al.*[10] c_{av} represents the mean speed of sound encountered by a wave propagating through the sample,

$$c_{av} = x/t = x\left(\int \frac{dx}{c_L(x)}\right)^{-1}. \tag{7}$$

Both $\overline{c_L}$ and c_{av} are reported.

https://doi.org/10.1121/10.0009316

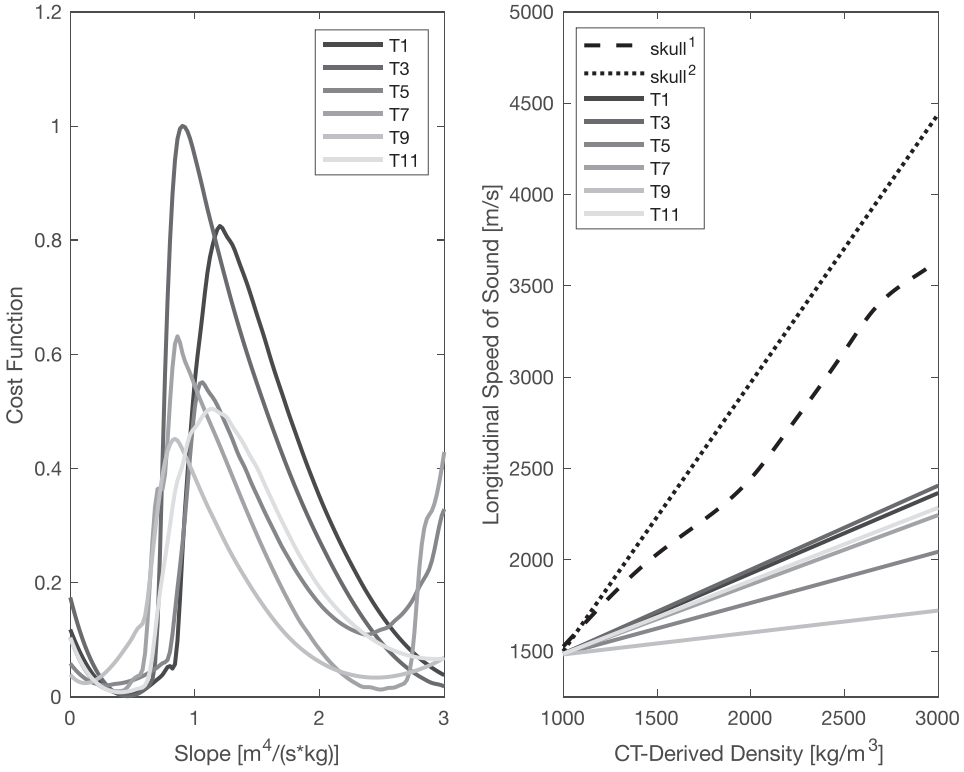

FIG. 11. Left, the cost functions for the tested linear models, and right, the linear models that correspond to the cost function minima. Two reference skull models are shown: (Ref. 1) the spline from Pichardo *et al.*, (Re. 11) interpolated to 514 kHz, and (Ref. 2) the linear model from Marsac *et al.* (Ref. 13) (1 MHz).

D. Simulated vs empirical time shifts

The error in simulated time shift is reported as a proportion of a 514 kHz wavelength in Table IV for the optimized linear vertebra model, $c_L(\rho) = 0.35(\rho - \rho_w) + c_{L,w}$. The errors are averaged across the five positions per vertebra and averaged across all vertebrae for the 'total' column. Figure 12 shows the experiment and simulation phases for all of the vertebrae and all of the experiments to provide a visualization of the errors reported in Table V.

The mean error of the mean vertebral model ($m = 0.35$) is 0.06λ, or $\lambda/16$. The phase shifts were also calculated using the initially used skull acoustic properties[11] and the mean error of the skull spline model used in Xu and O'Reilly[8] is 0.29λ, or $\lambda/3.5$. The accuracy of the linear models improves significantly on that of the skull spline model ($p = 0.04$), calculated with a one-tailed t-distribution.

E. Contributions of longitudinal and shear modes

Figure 13 displays the proportion of sound transmitted *via* the longitudinal and shear modes in terms of velocity magnitude at the vertebral canal interface, for each vertebra-transducer configuration. All simulations were performed with the optimized lamina $c_L(\rho)$ function. The amplitude of particle velocity at the simulated transducer surface was 1 m/s.

The mean amplitude of particle velocity propagated through the bone *via* the longitudinal mode averaged across all experiments was 0.53 ± 0.19 m/s, while the mean shear amplitude of particle velocity was 0.06 ± 0.04 m/s. The vertebrae show smoothly varying trends in amplitude of particle velocity, moving from experiment position 1 to 5, showing that the incident angles change with each 2.5 mm vertebra translation. T11 was the exception, perhaps due to its lumbar vertebra-like geometry and parabolic lamina resulting in a higher proportion of shear mode contributions for all positions. Figure 13 shows that longitudinal mode contributions generally dominate shear mode contributions, suggesting that the incident angles from the transducer are below the longitudinal critical angle.

The mean and bulk vertebral shear sound speeds ($\overline{c_S}$, $c_{S,av}$) in vertebrae were calculated with the optimized vertebral linear function, $c_S(\rho) = 0.19\rho + 810$ m/s. See Table VI.

TABLE III. Mean vertebra density in the posterior arch for two density thresholds ($\rho \geq 998$ or $\rho \geq 1200$ kg/m^3), cost function minima ($\Phi_{\min}$), and optimal slopes m ($\Phi_{\min}$). The value following the mean in the "Total" column is the standard deviation.

	T1	T3	T5	T7	T9	T11	Total
$\rho \geq = 1200$	1750	1727	1767	1782	1767	1695	1750 ± 30
$\rho \geq = 998$	1553	1579	1609	1621	1628	1592	1600 ± 30
$\Phi_{\min}(\times 10^{-3})$	4.0	1.2	20	9.9	24	8.1	11 ± 9
m ($\Phi_{\min}$)	0.44	0.46	0.28	0.38	0.12	0.40	0.35 ± 0.13

IV. DISCUSSION

In this work, empirical vertebra-induced group time shifts were measured from the odd-numbered thoracic

TABLE IV. Mean and bulk vertebral sound speed ($\overline{c_L}$, c_{av}) from the vertebral linear model for $\rho \geq 998$ kg/m^3 and $\rho \geq 1200$ kg/m^3.

$\overline{c_L}$ [m/s]		c_{av} [m/s]	
$\rho \geq 998$	$\rho \geq 1200$	$\rho \geq 998$	$\rho \geq 1200$
1690 ± 70	1740 ± 90	1670 ± 60	1730 ± 90

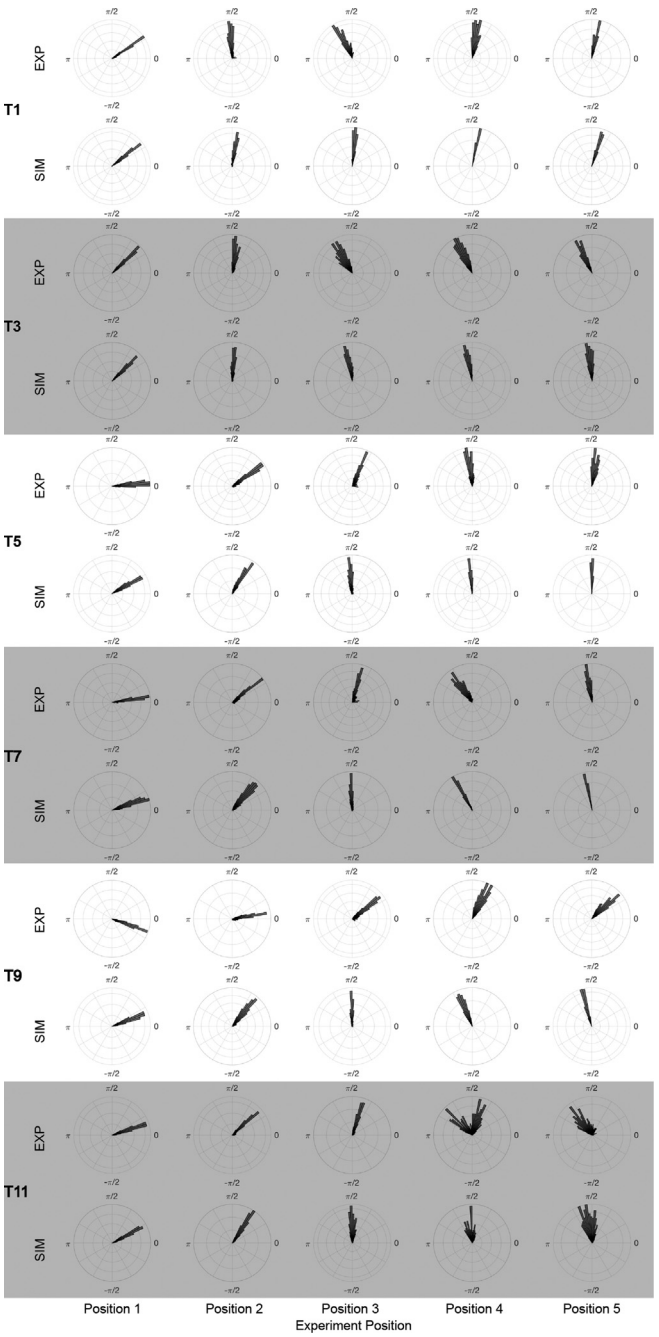

FIG. 12. Experimentally measured and simulated (ray acoustics with the mean optimal vertebral model) phases in voxels that exceed 50% of the intensity maximum.

vertebrae (T1, T3,… T11) from a single *ex vivo* human spine at body temperature (37 °C). The time shifts were extracted *via* normalized cross correlation of the signals produced by a single spherically focused transducer, driven with a 514 kHz single cycle, measured in a three-dimensional (3D) volume in water then measured in the same 3D volume in the vertebral canals of the vertebrae. The vertebra-induced time shifts measured in this work (displayed in Fig. 7, and summarized in Table I) were bounded within $[\pi/4, -\pi]$ radians. This range of time shifts allowed the multi-layered ray acoustics model to be used to optimize

TABLE V. Mean vertebral linear model errors and standard deviations (σ) in errors in calculated vertebra-induced time shifts.

	T1	T3	T5	T7	T9	T11	Total
Error [λ]	0.03	0.04	0.07	0.05	0.14	0.05	0.06
σ	0.02	0.03	0.05	0.03	0.03	0.02	0.05

$c_L(\rho)$ functions without concerns about phase wrapping. The ability to use simulation was paramount, as lamina thickness alone did not sufficiently explain the empirically measured time shifts. The range of vertebra-induced time shifts suggest that the shear mode occasionally contributes significantly to transvertebral ultrasound propagation. Some vertebra-induced time shifts were positive, which corresponds to a slower sound speed than in water. This effect is seen in shear mode propagation. Shear mode propagation can be dominant when the incident angles are high, e.g., when the ultrasound beam intercepts the superior or inferior curved edges of the laminae. The simulation model accuracy was tested using skull acoustic properties prior to any vertebral sound speed optimization in order to ensure that the input experimental data and vertebra registration in simulation were of sufficient accuracy. The slices through the geometric focus of the transducer displayed in Fig. 10 show the pressure profiles of all of the tested transducer-vertebra configurations. The total root mean square pressure error of the ray acoustics simulation was lower than reported in Xu and O'Reilly,[8] and the zero-lag cross correlation of the ray acoustics simulation was higher than reported in Xu and O'Reilly, confirming that the experimental data and vertebra registrations were accurate.

The interference between longitudinal and shear modes has previously been investigated by Modena *et al.* in skulls,[52] and the shear and longitudinal waves may interfere in a similar manner to the "fast" and "slow" waves that have previously been investigated[53,54] and that have been reported to generate negative dispersion in bone when the interfered signals are analyzed as a single signal. The waveforms acquired in this work were analyzed as single waveforms without interference between slow and fast waves or shear and longitudinal waves, as the signals in the maximum pressure region [Fig. 4(b)] did not display the characteristic mixed waveform seen in prior work with separable fast and slow waves.[53,55–57] This may be an indication that sound transmission through the lamina was orthogonal to the trabecular orientation, as fast-slow wave separation is usually seen when sound transmission is along the trabeculae.[31]

An important finding was the differences in group time shifts that resulted from relatively small (2.5 mm) vertical vertebra shifts. Changes in group time shifts were correlated with changes in lamina thickness, as they are in skull,[58] and a linear fit suggested that bulk sound speed in the vertebral lamina was slow, approximately 1650 m/s for the median lamina thickness. However, the range of time shifts around the linear fit was high, likely originating from the irregularity of the laminae; a small change in vertebra position

https://doi.org/10.1121/10.0009316

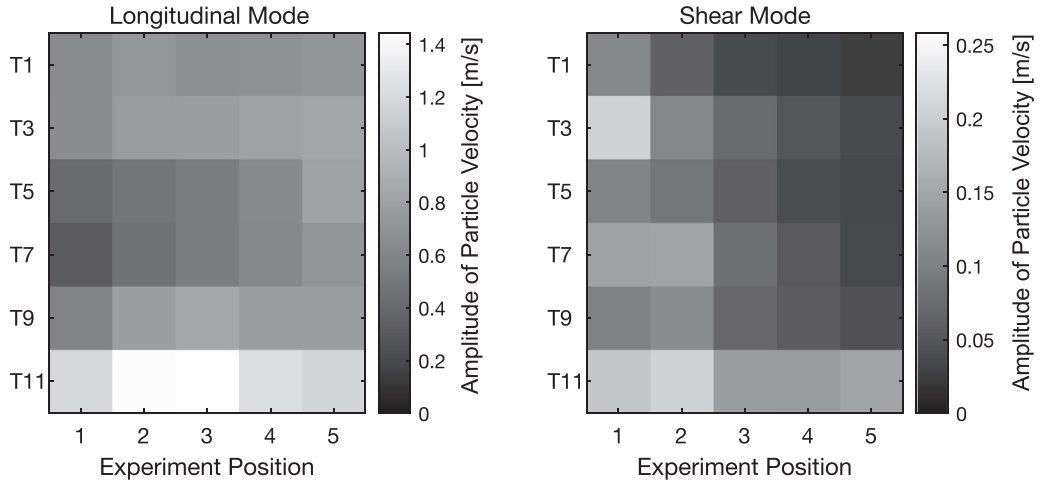

FIG. 13. Sound transmission through the lamina to the vertebral canal *via* longitudinal vs and shear modes, calculated using the optimized linear models. The vertebrae were shifted 2.5 mm vertically (z) between each experiment position, changing the incident angles and the ratio of shear to longitudinal transmission.

changes the ultrasound incident angles, changing the longitudinal and shear transmission coefficients and the corresponding shear and longitudinal contributions to the sound that reaches the vertebral canal. Figure 13 supports this finding by showing that the shear and longitudinal contributions change drastically but smoothly over the 10 mm range of vertebra positions. The low correlation between vertebra-induced time shift and lamina thickness and the variability in shear and longitudinal contributions highlight the need for a simulation-based optimization approach that accounts for both longitudinal and shear modes.

The irregular shape and variable density and corresponding acoustic properties precluded the use of bulk acoustic property measurement techniques.[36,37] Instead, a multi-layered ray acoustics model was applied that accounts for medium heterogeneities to optimize a set of linear functions that relate CT-derived density to the longitudinal speed of sound. These linear functions were optimized by minimizing a cost function [Eq. (5)] based on a pressure-weighted sum of simulation phase errors relative to empirical measurements. The ray acoustics model is similar to the mesh-based propagation model in Pichardo *et al.*,[11] although the method implemented here uses less spatial smoothing along the path of the rays in bone, solely taking the value of the closest voxels along the ray rather than averaging on the plane orthogonal to the ray at each step.

The density distribution of the vertebrae included all values from within the mask segmented from the vertebra (Fig. 1). This means that large pores within the trabecular structure are incorporated into the density estimate, causing partial volume effects. We reported bulk densities and bulk speeds of sound for two thresholds: $\rho > 1200$ kg/m^3 for comparison with Pichardo *et al.*[11] and $\rho > 998$ kg/m^3 to include all voxels within the bone mesh and report the bulk density for the entire bone. The mean density for $\rho > 1200$ kg/m^3 was 1750 ± 50 kg/m^3, approximately 160 kg/m^3 less than in the value reported in Pichardo *et al.*[11] (different CT scanner and reconstruction kernel) and approximately 90 kg/m^3 less than Fry and Barger.[9] Further improvements in density accuracy could be obtained using a bone mineral density phantom. McDannold *et al.*[15] includes skulls imaged with the same CT scanner and beam energy but reports the skull density ratio rather than the bulk density. The low density measured in the vertebral lamina may possibly be due to aging, as the spine is a primary site for bone loss during aging.[59] Figure 1 also shows that the cortical shell density of the lamina is much higher than the density of the internal trabeculae, and this could have similar implications to the skull density ratio used to estimate the transmission efficiency through skull.[60]

TABLE VI. Mean and bulk vertebral lamina shear sound speed ($\overline{c_S}$, $c_{S,av}$) calculated with the vertebral linear model at $\rho \geq 998$ kg/m^3 and $\rho \geq 1200$ kg/m^3.

$\overline{c_S}$ [m/s]		$c_{S,av}$ [m/s]	
$\rho \geq 998$	$\rho \geq 1200$	$\rho \geq 998$	$\rho \geq 1200$
930 ± 40	950 ± 50	920 ± 40	950 ± 50

A. Comparison of linear models

The mean increase in sound speed per unit of CT-derived density (slope, m) for the optimized linear model was 0.35 m^4/(s kg), giving $c_L(\rho) = 0.35(\rho - \rho_w) + 1481$ m/s. The optimal linear model performed significantly better in reproducing vertebra-induced phase shifts than the skull spline model from Pichardo *et al.*,[11] with an accuracy of $\lambda/16$ instead of $\lambda/3.5$. The slopes of the linear models were lower than the model obtained for skull at 510 kHz in Clement and Hynynen,[58] $c_L(\rho) = 2.06\rho - 1540$ m/s, although the model from Ref. 58 intercepts a much lower speed of sound at the density of water (520 m/s). The optimized linear models were slower than that of Aubry *et al.*[61] and Marquet *et al.*,[62] which is slower than that of Marsac *et al.*[13] (shown in Fig. 11). These studies were performed at

1 MHz[13,62] and 1.5 MHz[61] and dispersion may result in different sound speeds at these frequencies, although unlikely to make a difference of hundreds of meters per second. Webb *et al.*[14] reports the relationship between CT Hounsfield units and speed of sound with various x-ray energies and reconstruction methods with results that were generally in agreement with.[61] Of the studies that linearly relate the speed of sound in skull with CT-derived density, all report faster sound speeds than found in this work for vertebral lamina. This finding may be due to trabecular anisotropy, where the trabecular orientation may be orthogonal to the ultrasound propagation direction, and possible differences in the microstructure of cortical bone.

B. Comparison of bulk lamina values to skull

Large differences in the linear $c_L(\rho)$ functions optimized for skull versus those optimized here for the vertebral posterior arch were found. When these optimized models were applied to the CT-density derived data, the resultant arithmetic mean speeds of sound ($\overline{c_L}$) and bulk speeds of sound (c_{av}) in the vertebral laminae were much lower than those in skull. For example, the bulk speed of sound in skull and reported by Pichardo *et al.*,[11] interpolated to 514 kHz is 2341 ± 140 m/s. The arithmetic mean speeds of sound in the lamina reported for the vertebrae tested in this experiment and fit with the mean optimal linear model were approximately 600 m/s slower than that which were reported by Pichardo *et al.*[11] for skull ($p = 0.009$, calculated with a two-tailed T-test). The decrease in bulk speed of sound in the vertebrae relative to the bulk speed of sound in skull[11] exceeds the 500 m/s range of variation in speed of sound with respect to trabecular orientation measured by Nicholson *et al.*[28] in vertebral bodies. Several other studies have reported bulk longitudinal speed of sound measurements in skull.[9,10,39,63,64] The bulk phase velocity for a pulse centered at 550 kHz reported by Fry and Barger[9] for full skulls is 2337 m/s, while the group velocity measured by a transit time method is 2740 ± 140 m/s. Other works found even faster sound speeds. The average longitudinal speed of sound skull bone measured using a bulk measurement technique at 1 MHz in White *et al.*[39] is 2820 ± 40 m/s. Connor *et al.*[10] found a range of sound speeds (2610–2885 m/s), although this study was performed at 740 kHz. Exceptions are McKelvie and Palmer,[65] who found sound speeds at 0.5 MHz in trabecular bone between 1688 and 2084 m/s, and similar to the range of bulk lamina sound speeds found here. Hans *et al.*[29] measured sound speed in trabecular cubes extracted from lumbar vertebrae, finding values between 1662 and 1715 m/s, depending on the orientation of the cube; similar sound speeds to those extracted here.

The results shown in Fig. 13 highlight the need to incorporate both longitudinal and shear mode propagation when simulating ultrasound propagation through the posterior arch, particularly in positions near the superior or inferior edge of the lamina. Most of the discussion here centers on the longitudinal speed of sound, as most prior work has focused on trans-skull propagation at normal incidence. However, some work has investigated the shear speed of sound in skull.[11,39] White *et al.* used a bulk measurement technique and found that the shear speed of sound was 1500 ± 140 m/s in *ex vivo* skulls,[39] very similar to the longitudinal speed of sound in water. However, the optimized bulk shear sound speed in the vertebral lamina was slower than the longitudinal speed of sound in water, and this was evidence by positive vertebra-induced time shifts in some transducer-vertebra positions, shown in Fig. 7.

C. Limitations

The analysis for the acoustic properties performed here was based solely on empirical measurements obtained from a set of thoracic vertebrae from a single spine of unknown age and sex. We assumed that the vertebrae used in this study were representative of an average human, and that the range of variation in vertebral morphology and density within a single thoracic column covered the range of variation between individual vertebrae in a population. However, age and sex-specific measurements may produce different optimal speed of sound functions due to loss in bone density with aging (particularly in the spine) and the corresponding changes trabecular trajectory architecture,[59] along with differences in vertebral morphology due to sexual dimorphism.[66] Additional measurements should be performed with vertebrae of known origin in order to confidently establish vertebral lamina sound speed models for the general population and to ensure the accuracy of transvertebral beamforming. Furthermore, in this study, we used clinical CT data with limited resolution. This was an intentional study design choice to generate a speed of sound model that was relevant for the clinical imaging data expected to be used in treatment planning. However, it would be helpful to have micro-CT images or deconvolution methods to recover thin cortical bone structures in the vertebra lamina to extract trabecular orientation and porosity of the bone and to estimate trabecular anisotropy;[67] Pal *et al.*[32] show a sparse trabecular network in the lamina,[33] but a quantitative analysis of the lamina trabecular architecture and anisotropy could provide further support for the low sound speeds extracted here. If deconvolution methods[67] to extract thin bone structures could be adapted to gain information regarding trabecular structure from low resolution CT, this could improve treatment planning models while still utilizing standard clinical CT datasets. A further limitation of the CT data is that it is not sensitive to collagen, which influences sound speed in both cortical[68] and trabecular[69] bone, which may degrade the model accuracy *in vivo*. The vertebrae used in this study were stored in 10% buffered formalin, which has been shown to have minimal effect on the acoustic properties of skull.[9] Experiments with fresh, dehydrated and formalin-fixed vertebrae should be performed to determine the acoustic effect of 10% buffered formalin on human vertebrae. The measurements performed in this study were performed at 37 °C, as previous work has observed a near-linear increase

in phase changes with temperatures between room temperature and 50 °C, although the total phase change in this range was reported to be less than 14° in skull.[58] A future study could test the temperature dependence of the sound speed in the vertebral lamina.

In this work, the shear sound speed was set as a fixed ratio of the longitudinal sound speed. The independent optimization of the shear sound speed could further improve the accuracy of the model in reproducing the empirical vertebra-induced time shifts.

Short pulse schemes for focusing ultrasound through the posterior arch of the vertebra and creating a controlled focus without generating standing waves have been developed.[47] One of these pulses (i.e., with zero phase-shift), when convolved with the transducer impulse response, will result in a signal with the bandwidth similar to that shown in Fig. 3. Bone and soft tissue are dispersive materials that generally follow a frequency power law,[53,54,70] and accurately accounting for the behaviour of a signal with a broader frequency content than a continuous wave propagating through bone and soft tissue requires a full wave simulation model. One such model is the pseudospectral method encoded in k-Wave; a well-accepted numerical model for time-domain ultrasound propagation in heterogeneous media that can account for dispersion and the transient nature of the trans-spine pulse schemes.[71,72] However, the suitable k-Wave model (`pstdElastic3D`) is significantly more computationally expensive than the ray acoustics model. For example, the elastic k-Wave code requires ∼2 h to simulate one transducer-vertebra configuration for the experiment domain size discretized to $\lambda/6$ and with a CFL of 0.05 on an Intel Xeon Silver 4114 processor, while the multi-layered ray acoustics model only requires 20–30 s with an NVIDIA RTX 2080 GPU. Further spatial discretization is likely necessary in the k-Wave model, further increasing the computational cost, although potentially enabling the simulation of ultrasound propagation through trabecular networks if the CT resolution is sufficiently high. The additional computational expense of the k-Wave elastic model makes it less suited to the optimization process necessary for generating an optimal $c_L(\rho)$ function for human thoracic vertebrae.

V. CONCLUSION

This study found that the longitudinal speed of sound for a given voxel density in the vertebral lamina of *ex vivo* thoracic vertebrae from a single human spine was slower than that of a voxel of equal density in skull. A linear model was optimized in this work, $c_L(\rho) = 0.35(\rho - \rho_w) + c_{L,w}$, at body temperature. The vertebra linear model provided a significant improvement ($\lambda/3.5$ to $\lambda/16$) in time domain accuracy over a spline model optimized for skull bone, for the tested vertebrae. The average CT-derived density of the vertebral laminae was lower than that of skull, giving lower bulk estimates of speed of sound relative to skull. The optimized vertebra-specific $c_L(\rho)$ models may improve the accuracy of trans-spine beamforming algorithms, particularly when focusing using an array that focuses sound both through the posterior vertebral arch and through the paravertebral acoustic windows.

ACKNOWLEDGMENTS

This study was funded by the NSERC Discovery, Ontario Ministry of Research, Innovation and Science Early Researcher Award, the Canada Foundation for Innovation John R. Evans Leaders Fund/Ontario Research Fund—Research Infrastructure, and Canada Research Chair Program, and the NSERC Postgraduate Scholarships Doctoral program.

[1]D. Weber-Adrian, E. Thévenot, M. A. O'Reilly, W. Oakden, M. K. Akens, N. Ellens, K. Markham-Coultes, A. Burgess, J. Finkelstein, A. J. Yee, C. M. Whyne, K. D. Foust, B. K. Kaspar, G. J. Stanisz, R. Chopra, K. Hynynen and I. Aubert, "Gene delivery to the spinal cord using MRI-guided focused ultrasound," Gene Therapy **22**(7), 568–577 (2015).
[2]A. H. Payne, G. W. Hawryluk, Y. Anzai, H. Odéen, M. A. Ostlie, E. C. Reichert, A. J. Stump, S. Minoshima, and D. J. Cross, "Magnetic resonance imaging-guided focused ultrasound to increase localized blood-spinal cord barrier permeability," Neural Regen. Res. **12**(12), 2045–2049 (2017).
[3]M. A. O'Reilly, T. Chinnery, M.-L. Yee, S.-K. Wu, K. Hynynen, R. S. Kerbel, G. J. Czarnota, K. I. Pritchard, and A. Sahgal, "Preliminary investigation of focused ultrasound-facilitated drug delivery for the treatment of leptomeningeal metastases," Sci. Rep. **8**(1), 1–8 (2018).
[4]S.-M. P. Fletcher, N. Ogrodnik, and M. A. O'Reilly, "Enhanced detection of bubble emissions through the intact spine for monitoring ultrasound-mediated blood-spinal cord barrier opening," IEEE Trans. Biomed. Eng. **67**, 1387–1396 (2020).
[5]S.-M. P. Fletcher, M. Choi, R. Ramesh, and M. O'Reilly, "Effect of sonication parameters on the efficacy of focused ultrasound and microbubble-mediated blood-spinal cord barrier opening using short-burst, phase keying exposures," J. Acoust. Soc. Am. **148**(4), 2799 (2020).
[6]P. Smith, N. Ogrodnik, J. Satkunarajah, and M. A. O'Reilly, "Characterization of ultrasound-mediated delivery of trastuzumab to normal and pathologic spinal cord tissue," Sci. Rep. **11**(1), 1–12 (2021).
[7]S.-M. P. Fletcher, M. Choi, N. Ogrodnik, and M. A. O'Reilly, "A porcine model of transvertebral ultrasound and microbubble-mediated blood-spinal cord barrier opening," Theranostics **10**(17), 7758–7774 (2020).
[8]R. Xu and M. A. O'Reilly, "Simulating transvertebral ultrasound propagation with a multi-layered ray acoustics model," Phys. Med. Biol. **63**(14), 145017 (2018).
[9]F. J. Fry and J. E. Barger, "Acoustical properties of the human skull," J. Acoust. Soc. Am. **63**(5), 1576–1590 (1978).
[10]C. W. Connor, G. T. Clement, and K. Hynynen, "A unified model for the speed of sound in cranial bone based on genetic algorithm optimization," Phys. Med. Biol. **47**(22), 3925–3944 (2002).
[11]S. Pichardo, V. W. Sin, and K. Hynynen, "Multi-frequency characterization of the speed of sound and attenuation coefficient for longitudinal transmission of freshly excised human skulls," Phys. Med. Biol. **56**(1), 219–250 (2011).
[12]S. Pichardo, C. Moreno-Hernández, R. Andrew Drainville, V. Sin, L. Curiel, and K. Hynynen, "A viscoelastic model for the prediction of transcranial ultrasound propagation: Application for the estimation of shear acoustic properties in the human skull," Phys. Med. Biol. **62**, 6938–6962 (2017).
[13]L. Marsac, D. Chauvet, R. L. Greca, A.-L. Boch, K. Chaumoitre, M. Tanter, and J.-F. Aubry, "Ex vivo optimisation of a heterogeneous speed of sound model of the human skull for non-invasive transcranial focused ultrasound at 1 mHz," Int. J. Hyperthermia **33**(6), 635–645 (2017).
[14]T. D. Webb, S. A. Leung, J. Rosenberg, P. Ghanouni, J. Dahl, N. J. Pelc, and K. B. Pauly, "Measurements of the relationship between ct hounsfield units and acoustic velocity and how it changes with photon energy and reconstruction method," IEEE Trans. Ultrason. Ferroelectr. Freq. Control **65**, 1111–1124 (2018).

[15]N. McDannold, P. J. White, and R. Cosgrove, "Elementwise approach for simulating transcranial mri-guided focused ultrasound thermal ablation," Phys. Rev. Res. **1**(3), 033205 (2019).
[16]K. Hynynen and F. A. Jolesz, "Demonstration of potential noninvasive ultrasound brain therapy through an intact skull," Ultrasound Med. Biol. **24**(2), 275–283 (1998).
[17]N. McDannold, N. Vykhodtseva, S. Raymond, F. A. Jolesz, and K. Hynynen, "MRI-guided targeted blood-brain barrier disruption with focused ultrasound: Histological findings in rabbits," Ultrasound Med. Biol. **31**(11), 1527–1537 (2005).
[18]N. McDannold, C. D. Arvanitis, N. Vykhodtseva, and M. S. Livingstone, "Temporary disruption of the blood–brain barrier by use of ultrasound and microbubbles: Safety and efficacy evaluation in rhesus macaques," Cancer Res. **72**(14), 3652–3663 (2012).
[19]G. F. Pinton, J.-F. Aubry, and M. Tanter, "Direct phase projection and transcranial focusing of ultrasound for brain therapy," IEEE Trans. Ultrason. Ferroelectr. Freq. Control **59**(6), 1149–1159 (2012).
[20]W. J. Elias, N. Lipsman, W. G. Ondo, P. Ghanouni, Y. G. Kim, W. Lee, M. Schwartz, K. Hynynen, A. M. Lozano, B. B. Shah, D. Huss, R. F. Dallapiazza, R. Gwinn, J. Witt, S. Ro, H. M. Eisenberg, P. S. Fishman,D. Gandhi, C. H. Halpern, R. Chuang, K. Butts Pauly, T. S. Tierney, M. T. Hayes, G. Rees Cosgrove, T. Yamaguchi, K. Abe, T. Taira, and J. W. Chang, "A randomized trial of focused ultrasound thalamotomy for essential tremor," New England J. Med. **375**(8), 730–739 (2016).
[21]G. Maimbourg, A. Houdouin, T. Deffieux, M. Tanter, and J.-F. Aubry, "3D-printed adaptive acoustic lens as a disruptive technology for transcranial ultrasound therapy using single-element transducers," Phys. Med. Biol. **63**(2), 025026 (2018).
[22]S. Jiménez-Gambín, N. Jiménez, J. M. Benlloch, and F. Camarena, "Holograms to focus arbitrary ultrasonic fields through the skull," Phys. Rev. Appl. **12**(1), 014016 (2019).
[23]A. E. Bond, B. B. Shah, D. S. Huss, R. F. Dallapiazza, A. Warren, M. B. Harrison, S. A. Sperling, X.-Q. Wang, R. Gwinn, J. Witt, S. Ro, and W. Jeffrey Elias, "Safety and efficacy of focused ultrasound thalamotomy for patients with medication-refractory, tremor-dominant Parkinson disease: A randomized clinical trial," JAMA Neurol. **74**(12), 1412–1418 (2017).
[24]N. Lipsman, Y. Meng, A. J. Bethune, Y. Huang, B. Lam, M. Masellis, N. Herrmann, C. Heyn, I. Aubert, A. Boutet, G. S. Smith, K. Hynynen and S. E. Black, "Blood–brain barrier opening in Alzheimer's disease using R-guided focused ultrasound," Nat. Commun. **9**(1), 1–8 (2018).
[25]Y. Meng, R. M. Reilly, R. C. Pezo, M. Trudeau, A. Sahgal, A. Singnurkar, J. Perry, S. Myrehaug, C. B. Pople, B. Davidson, , M. Llinas, C. Hyen, Y. Huang, C. Hamani, S.suppiah, K. Hynynen, and N. Lipsman, "Mr-guided focused ultrasound enhances delivery of trastuzumab to her2-positive brain metastases," Sci. Trans. Med. **13**(615), eabj4011 (2021).
[26]T. D. Webb, S. A. Leung, P. Ghanouni, J. J. Dahl, N. J. Pelc, and K. B. Pauly, "Acoustic attenuation: Multifrequency measurement and relationship to CT and MR imaging," IEEE Trans. Ultrason. Ferroelectr. Freq. Control **68**, 1532–1535 (2021).
[27]R. Xu and M. Anne O'Reilly, "A spine-specific phased array for transvertebral ultrasound therapy: Design & simulation," IEEE Trans. Biomed. Eng. **67**, 256–267 (2020).
[28]P. H. F. Nicholson, M. J. Haddaway, and M. W. J. Davie, "The dependence of ultrasonic properties on orientation in human vertebral bone," Phys. Med. Biol. **39**(6), 1013–1024 (1994).
[29]D. Hans, C. Wu, C. F. Njeh, S. Zhao, P. Augat, D. Newitt, T. Link, Y. Lu, S. Majumdar, and H. K. Genant, "Ultrasound velocity of trabecular cubes reflects mainly bone density and elasticity," Calcified Tissue Int. **64**(1), 18–23 (1999).
[30]N. Murashima, I. Michimoto, D. Koyama, and M. Matsukawa, "Anisotropic longitudinal wave propagation in swine skull," IEEE Trans. Ultrason. Ferroelectr. Freq. Control **68**, 65–71 (2021).
[31]K. A. Wear, "Mechanisms of interaction of ultrasound with cancellous bone: A review," IEEE Trans. Ultrason. Ferroelectr. Freq. Control **67**, 454–482 (2020).
[32]C. M. Gdyczynski, A. Manbachi, S. Hashemi, B. Lashkari, and R. S. C. Cobbold, "On estimating the directionality distribution in pedicle trabecular bone from micro-CT images," Physiol. Meas. **35**(12), 2415–2428 (2014).
[33]G. P. Pal, L. Cosio, and R. V. Routal, "Trajectory architecture of the trabecular bone between the body and the neural arch in human vertebrae," Anatomical Rec. **222**(4), 418–425 (1988).
[34]G. P. Pal and R. V. Routal, "The role of the vertebral laminae in the stability of the cervical spine," J. Anatomy **188**, 485–489 (1996).
[35]C. M. Whyne, S. S. Hu, S. Klisch, and J. C. Lotz, "Effect of the pedicle and posterior arch on vertebral body strength predictions in finite element modeling," Spine **23**(8), 899–907 (1998).
[36]P. H. F. Nicholson, G. Lowet, C. M. Langton, J. Dequeker, and G. Van der Perre, "A comparison of time-domain and frequency-domain approaches to ultrasonic velocity measurement in trabecular bone," Phys. Med. Biol. **41**(11), 2421–2435 (1996).
[37]J. J. Kaufman, W. Xu, A. E. Chiabrera, and R. S. Siffert, "Diffraction effects in insertion mode estimation of ultrasonic group velocity," IEEE Trans. Ultrason. Ferroelectr. Freq. Control **42**(2), 232–242 (1995).
[38]R. Shahar, P. Zaslansky, M. Barak, A. A. Friesem, J. D. Currey, and S. Weiner, "Anisotropic Poisson's ratio and compression modulus of cortical bone determined by speckle interferometry," J. Biomech. **40**(2), 252–264 (2007).
[39]P. Jason White, G. T. Clement, and K. Hynynen, "Longitudinal and shear mode ultrasound propagation in human skull bone," Ultrasound Med. Biol. **32**(7), 1085–1096 (2006).
[40]R. M. Jones, M. A. O'Reilly, and K. Hynynen, "Transcranial passive acoustic mapping with hemispherical sparse arrays using ct-based skull-specific aberration corrections: A simulation study," Phys. Med. Biol. **58**(14), 4981–5005 (2013).
[41]P. J. White, S. Palchaudhuri, K. Hynynen, and G. T. Clement, "The effects of desiccation on skull bone sound speed in porcine models," IEEE Trans. Ultrason. Ferroelectr. Frequ. Control **54**(8), 1708–1710 (2007).
[42]W. Limthongkul, E. E. Karaikovic, J. W. Savage, and A. Markovic, "Volumetric analysis of thoracic and lumbar vertebral bodies," Spine J. **10**(2), 153–158 (2010).
[43]N. Lipsman, M. L. Schwartz, Y. Huang, L. Lee, T. Sankar, M. Chapman, K. Hynynen, and A. M. Lozano, "Mr-guided focused ultrasound thalamotomy for essential tremor: A proof-of-concept study," Lancet Neurol. **12**(5), 462–468 (2013).
[44]D. Dragomir-Daescu, C. Salas, S. Uthamaraj, and T. Rossman, "Quantitative computed tomography-based finite element analysis predictions of femoral strength and stiffness depend on computed tomography settings," J. Biomech. **48**(1), 153–161 (2015).
[45]H. Montanaro, C. Pasquinelli, H. J. Lee, H. Kim, H. R. Siebner, N. Kuster, A. Thielscher, and E. Neufeld, "The impact of ct image parameters and skull heterogeneity modeling on the accuracy of transcranial focused ultrasound simulations," J. Neural Eng. **18**(4), 046041 (2021).
[46]M. E. Launey, M. J. Buehler, and R. O. Ritchie, "On the mechanistic origins of toughness in bone," Annu. Rev. Mater. Res. **40**, 25–53 (2010).
[47]S.-M. P. Fletcher and M. A. O'Reilly, "Analysis of multifrequency and phase keying strategies for focusing ultrasound to the human vertebral canal," IEEE Trans. Ultrason. Ferroelectr. Freq. Control **65**(12), 2322–2331 (2018).
[48]K. A. Wear, C. Baker, and P. Miloro, "Directivity and frequency-dependent effective sensitive element size of needle hydrophones: Predictions from four theoretical forms compared with measurements," IEEE Trans. Ultrason. Ferroelectr. Freq. Control **65**(10), 1781–1788 (2018).
[49]F. Viola and W. F. Walker, "A comparison of the performance of time-delay estimators in medical ultrasound," IEEE Trans. Ultrason. Ferroelectr. Freq. Control **50**(4), 392–401 (2003).
[50]P. Hasgall, F. D. Gennaro, C. Baumgartner, E. Neufeld, M. C. Gosselin, D. Payne, A. Klingenböck, and N. Kuster, "IT'IS database for thermal and electromagnetic parameters of biological tissues version 3.0," https://itis.swiss/virtual-population/tissue-properties/database/ (2015) (last accessed 3 August 2018).
[51]H. B. Mitchell, *Image Fusion: Theories, Techniques and Applications* (Springer Science & Business Media, New York, 2010).
[52]D. Modena, M. Baragona, D. Bošnački, B. J. T. Breuer, A. Elevelt, R. T. H. Maessen, P. A. J. Hilbers, and H. M. M. Ten Eikelder, "Modeling the interference between shear and longitudinal waves under high intensity focused ultrasound propagation in bone," Phys. Med. Biol. **63**(23), 235024 (2018).
[53]K. R. Marutyan, M. R. Holland, and J. G. Miller, "Anomalous negative dispersion in bone can result from the interference of fast and slow waves," J. Acoust. Soc. Am. **120**(5), EL55–EL61 (2006).
[54]C. C. Anderson, K. R. Marutyan, M. R. Holland, K. A. Wear, and J. G. Miller, "Interference between wave modes may contribute to the apparent

negative dispersion observed in cancellous bone," J. Acoust. Soc. Am. **124**(3), 1781–1789 (2008).
[55]A. Hosokawa, T. Otani, T. Suzaki, Y. Kubo, and S. Takai, "Influences of trabecular structure on ultrasonic wave propagation in bovine cancellous bone," Jpn. J. Appl. Phys. **36**(5S), 3233–3237 (1997).
[56]E. Bossy, F. Padilla, F. Peyrin, and P. Laugier, "Three-dimensional simulation of ultrasound propagation through trabecular bone structures measured by synchrotron microtomography," Phys. Med. Biol. **50**(23), 5545–5556 (2005).
[57]M. Fellah, Z. El Abiddine Fellah, F. G. Mitri, E. Ogam, and C. Depollier, "Transient ultrasound propagation in porous media using biot theory and fractional calculus: Application to human cancellous bone," J. Acoust. Soc. Am. **133**(4), 1867–1881 (2013).
[58]G. T. Clement and K. Hynynen, "Correlation of ultrasound phase with physical skull properties," Ultrasound Med. Biol. **28**(5), 617–624 (2002).
[59]B. L. Riggs, H. W. Wahner, W. L. Dunn, R. B. Mazess, K. P. Offord, and L. J. Melton III, "Differential changes in bone mineral density of the appendicular and axial skeleton with aging: Relationship to spinal osteoporosis," J. Clin. Investig. **67**(2), 328–335 (1981).
[60]W. S. Chang, H. H. Jung, E. Zadicario, I. Rachmilevitch, T. Tlusty, S. Vitek, and J. W. Chang, "Factors associated with successful magnetic resonance-guided focused ultrasound treatment: Efficiency of acoustic energy delivery through the skull," J. Neurosurg. **124**(2), 411–416 (2016).
[61]J.-F. Aubry, M. Tanter, M. Pernot, J.-L. Thomas, and M. Fink, "Experimental demonstration of noninvasive transskull adaptive focusing based on prior computed tomography scans," J. Acoust. Soc. Am **113**(1), 84–93 (2003).
[62]F. Marquet, M. Pernot, J.-F. Aubry, G. Montaldo, L. Marsac, M. Tanter, and M. Fink, "Non-invasive transcranial ultrasound therapy based on a 3d ct scan: Protocol validation and in vitro results," Phys. Med. Biol. **54**(9), 2597–2613 (2009).
[63]B. Martin and J. H. McElhaney, "The acoustic properties of human skull bone," J. Biomed. Mater. Res. **5**(4), 325–333 (1971).
[64]A. D. Francis, *Physical Properties of Tissues: A Comprehensive Reference Book* (Academic Press, New York, 1990).
[65]M. L. McKelvie and S. B. Palmer, "The interaction of ultrasound with cancellous bone," Phys. Med. Biol. **36**(10), 1331–1340 (1991).
[66]M. Bastir, A. Higuero, L. Ríos, and D. G. Martínez, "Three-dimensional analysis of sexual dimorphism in human thoracic vertebrae: Implications for the respiratory system and spine morphology," Am. J. Phys. Anthropol. **155**(4), 513–521 (2014).
[67]A. Pakdel, M. Hardisty, J. Fialkov, and C. Whyne, "Restoration of thickness, density, and volume for highly blurred thin cortical bones in clinical ct images," Ann. Biomed. Eng. **44**(11), 3359–3371 (2016).
[68]S. S. Mehta, O. K. Öz, and P. P. Antich, "Bone elasticity and ultrasound velocity are affected by subtle changes in the organic matrix," J. Bone Miner. Res. **13**(1), 114–121 (1998).
[69]B. K. Hoffmeister, S. A. Whitten, S. C. Kaste, and J. Y. Rho, "Effect of collagen and mineral content on the high-frequency ultrasonic properties of human cancellous bone," Osteoporosis Int. **13**(1), 26–32 (2002).
[70]P. Droin, G. Berger, and P. Laugier, "Velocity dispersion of acoustic waves in cancellous bone," IEEE Trans. Ultrason. Ferroelectr. Freq. Control **45**(3), 581–592 (1998).
[71]B. E. Treeby and B. T. Cox, "k-wave: MATLAB toolbox for the simulation and reconstruction of photoacoustic wave fields," J. Biomed. Opt. **15**(2), 021314 (2010).
[72]B. E. Treeby, J. Jaros, D. Rohrbach, and, and B. T. Cox, "Modelling elastic wave propagation using the k-wave MATLAB toolbox," in Proceedings of the 2014 IEEE International Ultrasonics Symposium, Chicago, IL (September 3–6, 2014), pp. 146–149.